PHOTONICS Research

Broadband infinite-*Q* plasmons enable intense Smith–Purcell radiation

Zi-Wen Zhang,[1,2] Chao-Hai Du,[1,2,*] Yu-Lu Lei,[2] Juan-Feng Zhu,[3] and Pu-Kun Liu[2]

[1]Center for Carbon-based Electronics, School of Electronics, Peking University, Beijing 100871, China
[2]State Key Laboratory of Advanced Optical Communication Systems and Networks, School of Electronics, Peking University, Beijing 100871, China
[3]Science, Mathematics and Technology (SMT), Singapore University of Technology and Design, Singapore 487372, Singapore
*Corresponding author: duchaohai@pku.edu.cn

Received 5 July 2023; revised 1 August 2023; accepted 1 September 2023; posted 5 September 2023 (Doc. ID 499770); published 1 November 2023

With the rapid development of nanophotonics for enhancing free-electron radiation, bound states in the continuum (BICs) have emerged as a promising approach for emitting intense Smith–Purcell radiation (SPR) with enhanced intensity. However, current BIC-based methods are limited to single-frequency operation, thereby restricting their applications requiring spectral and angular tunability, such as particle detectors and light sources. To overcome this limitation, this work proposes an approach for constructing plasmonic BICs over a broad spectral range in symmetry-broken systems. By leveraging the high-*Q* resonances near the BICs, we achieve intense SPR with broadband tunability, potentially improving the radiation intensity by six orders compared to traditional methods. Experimentally, we validate the construction of BIC using plasmonic antennas and achieve broadband demonstration. Our proposed concept can be extended to other plasmonic or guided-wave systems, paving the way toward compact and efficient free-electron sources in hard-to-reach frequency regimes.

https://doi.org/10.1364/PRJ.499770

1. INTRODUCTION

Smith–Purcell radiation (SPR) is one of the cathodoluminescence emissions, where the broadband and far-field Bloch photons are emitted as the charged particle traveling parallel to a periodic transparent medium or structure [1]. Notably, SPR has enabled numerous promising applications including beam diagnosis without destruction, free-electron lasers, and spectrally tunable light sources by virtue of its potential to emit photons at hard-to-reach frequencies comprising terahertz (THz), far-infrared, ultraviolet, and X-rays regimes [2–4]. However, due to the limited emission efficiency in achieving compact light sources, considerable efforts of the community have been devoted to achieving intense SPR by introducing photonic and plasmonic resonances, such as resonant cavity and surface plasmon polaritons (SPPs) [5,6]. Recent advances in metamaterial and nanophotonics manifest the capability and fortune to customize the polarization, phase, angular, spectral, and spatial distribution as well as to improve the radiation power of free-electron radiation [7]. For instance, the polarization state of SPR could be controlled based on Babinet, graphene, and gradient bianisotropic metasurfaces [8–10]. The phase distributions of SPR can be shaped into helical wavefronts by utilizing the helical or holographic grating, thus permitting the generation of vortex free-electron radiation [11–14]. Spectral-governable SPR has also been proposed in aperiodic gratings to engineer multiple peaks in the spectrum [15,16]. By elaborately designing the interaction circuit, the spatial distribution of SPR could be steered and focused based on chirped gratings or metasurfaces [17,18]. In addition to the aforementioned beam steering, the radiation power of Cherenkov radiation and SPR could be enhanced by plasmonic metamaterials or optical cavities due to the field enhancement of resonances, where the bound state in the continuum (BIC) has received prompt attention for being a novel approach to achieve intense SPR [19–24].

Ever since its first prediction in quantum mechanics in 1929, the BIC has been identified as a general wave phenomenon in photonic, phononic, and mechanic systems [25,26]. Although residing inside the continuum spectra where the extended states exist, the BIC does not couple to any of them and remains completely localized or bounded without any leakage, thereby theoretically allowing an infinite quality factor Q and a vanished resonant width in the spectrum [27–29]. Techniques developed to enhance the light–matter interaction by merit of BIC have spurred rapid photonic advancements, not only in high-Q applications including lasers, sensors, and antennas, but also in the exploration of silicon-based nanophotonic circuits and quantum information processing [30–34]. This close relationship between high-Q and artificial structures continues with the development of the BIC-enabled metamaterial, such

as the photonic crystal slab and fibers, in which the enhancement of the free-electron radiation is achieved [35]. The symmetry-protected BIC existing at the Γ-point of photonic crystal generates enhanced SPR by coupling electrons with BIC, demonstrating the universal upper limit to the photon emission and energy loss from free electrons [5]. According to the light-amplification process, the resonance-coupled BICs of the periodic silicon grating are engaged in a narrow spectral band to improve the efficiency of the SPR [36]. However, the BICs they utilized only exist at a single frequency point, limiting their ability to achieve continuous coupling of electrons with BICs over a wide spectral range while tuning electron energy. This restriction hinders the generation of intense SPR with broadband tunability, which poses challenges for developing compact free-electron lasers and charged particle detectors that require both spectral and angular tunability. Additionally, flatband resonance has also been employed to enhance the SPR, demonstrating an enhancement of radiation intensity by about two orders of magnitude [4]. Nonetheless, similar to the challenges faced with BIC enhancement, flatband resonance can only be constructed and coupled with the electron beam within a very narrow frequency band, limiting its applicability for broader tunability requirements. Hence, in the current approaches used to enhance SPR radiation, achieving wideband tunability remains a challenge. However, broad tunability is crucial for developing tunable light sources or detectors that need to operate over a broad spectrum. To address this limitation, spoof surface polaritons (SSPs) have emerged as a promising candidate to enable broadband BICs. Leveraging this approach allows us to achieve broadband coupling of the electron beam with BICs, leading to tunable intense Smith–Purcell radiation across a wide spectral range [23,37].

This work presents a methodology to design symmetry-protected broadband BICs from resonant SPPs, enabling intense SPR over a wide operating bandwidth. To construct BICs over the broadband range, we invoke the regular SSPs folding at the Brillouin band edge and block the leakage channel based on the Brillouin-folding phenomenon. When the phase-matching conditions are met between the free electrons and high-Q quasi-BICs, intense SPR with customizable spectral-angular distribution is generated. The performance of the generated radiation is validated in terms of tunability and enhancement. Compared with conventional schemes, the radiation intensity of BIC-enhanced SPR is about 10^6 times stronger due to the sharp high-Q resonances. The feasibility of the proposed BIC is also experimentally verified using plasmonic antennas in the microwave regime. Our approach provides a direct and promising way to enhance SPR using broadband BICs, which may be combined with foundry-based silicon photonics for the next generation of integrated and compact free-electron lasers [33,37].

2. RESULTS

A. Broadband Symmetry-Protected BIC from Resonant SSPs

Beginning with the illustration in Fig. 1, we concisely present the scheme and features of the proposed intense SPR. By modulating the depth of a double-slot 2D plasmonic grating, the symmetry-protected BICs are constructed from resonant SSPs in a broadband spectrum. Such SSP-based BICs have a theoretically infinite Q and a vanished resonant width, where the strong field enhancement of quasi-BICs near the BICs is then employed to emit intense SPR. When the sheet e-beam skims over the circuit and meets the phase-matching condition, the intense SPR with radiation intensity 10^6 times stronger than the regular one is generated, as indicated by the right insets of Fig. 1. To facilitate the discussion of the formation of such SSP-based BICs and the generation of intense SPR, it is essential to characterize the dispersion of the depth-modulated grating. As shown in the left inset of Fig. 1, the propagation and modulation periods of the system are d and $L = 2d$, respectively. The widths of both slots are $a = 0.4d$, whereas their depths are h_1 and h_2. In addition, the overall thickness of the grating is $h_3 = d$; thus, both h_1 and h_2 should be smaller than h_3. For the sake of analysis, the depth h_1 is fixed at $0.8d$ while the depth h_2 is increased from h_1 to h_3 during the modulation of the slot depth. Furthermore, the grating is modeled as a perfect electric conductor, neglecting any possible losses. For the 2D scheme (periodic in z), the TM modes without y

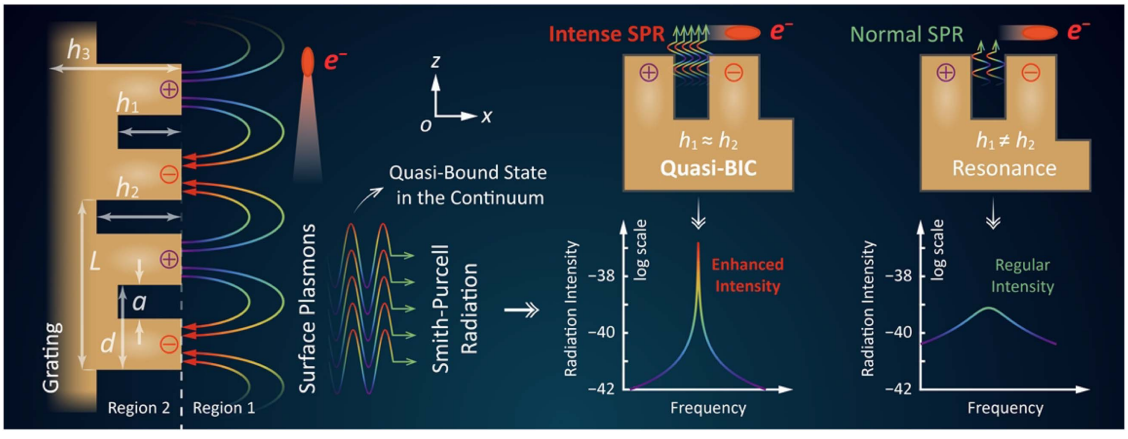

Fig. 1. Illustration of intense Smith–Purcell radiation from symmetry-protected BICs. By elaborately customizing the depth-modulated grating, the BICs are constructed from SSPs over a broad frequency range and are then employed to emit intense Smith–Purcell radiation. Compared with the conventional one, the radiation intensity of BIC-enhanced SPR is increased by several orders of magnitude.

dependency are considered, where the field extends to infinity in the $+x$ direction. Based on the mode-matching method, the eigenvalue equation of the depth-modulated grating is derived, and the dispersion relations could be solved numerically by [38]

$$|\mathbf{M}| = 0. \tag{1}$$

For a double-slot grating, $\mathbf{M}$ is a 2 × 2 matrix, with the element being

$$M(l, l') = X_{l,l'} - \delta(l - l')Y_l, \tag{2}$$

$$X_{l,l'} = \sum_{n=-\infty}^{\infty} \frac{k_0}{\tau_n} e^{-jk_{z0}(l-l')d} e^{jk_{zn}(l-l')d} Sa^2 \frac{k_{zn}a}{2}, \tag{3}$$

$$Y_l = \frac{L}{a} \cot k_0 h_l, \tag{4}$$

where both l and l' denote the slot numbers of the gratings in the system and should be less than two for a double-slot grating, n is the order of space harmonic, k_0 is the free-space wavenumber, τ_n is the transverse decaying factor, and the longitudinal wave vector $k_{zn} = k_{z0} + 2n\pi/L$. In addition to this, to accurately evaluate the asymmetry of the grating, it is essential to characterize the asymmetry parameter, which yields

$$\alpha = \frac{h_2 - h_1}{h_3 - h_1}, \quad h_1 < h_3, \quad h_1 \le h_2 \le h_3, \tag{5}$$

where the defined asymmetry parameter $\alpha \in [0, 1)$. The relation $\alpha = 0$ holds only when the depths of two slots are equal, $h_1 = h_2$; otherwise, $\alpha \neq 0$ when $h_1 \neq h_2$.

In the following, we will present the principle behind the formation of symmetry-protected BICs by examining the evolution of the dispersion relations at various asymmetry parameters α. As illustrated in the second row of Fig. 2, when α gradually increases from zero and then gradually decreases to zero, the dispersion relations of SSPs of the depth-modulated grating are numerically calculated according to Eq. (1). In contrast, the first row of Fig. 2 indicates the structural illustrations for different asymmetry parameters α. The frequency and wavenumber are normalized into dimensionless units $\omega L/2\pi c$ and $k_z L/2\pi$, in which c is the speed of light in vacuum. The yellow-shaded area is the fast wave region or light cone, while the white one is the slow wave region.

First, as indicated by Fig. 2(a), when the depths of the two slots are the same, $h_1 = h_2$, the grating is symmetric in one modulation period. Thus, asymmetry parameter $\alpha = 0$ holds according to Eq. (5). The two slots within one modulation period are identical. Therefore, the genuine period of the double-slot grating is no longer the modulation period L but the propagation period d. To accurately describe the actual minimum period of the grating during depth modulation, the genuine period is defined as p, in which the relation $p = d$ is established for $\alpha = 0$. The dispersion of the SSP supported by this symmetric grating is depicted as the black solid line in Fig. 2(a), which is exactly the one describing the regular SSPs.

Second, as illustrated by Fig. 2(b), once both h_2 and α increase, i.e., $h_1 < h_2$ and $\alpha \neq 0$, the dispersion distribution is changed accordingly due to the Brillouin-folding phenomenon. Since the two slots have different depths, the two propagation periods within a single modulation period are no longer equivalent. Therefore, the genuine period of the grating should be the modulation period, $p = L$, which is twice that of the symmetry one. According to Floquet's theorem for the periodic system with period p, the dispersion curve should also be periodically distributed in ω–k_{zn} space with $2\pi/p$ as the period, i.e., the ω is a periodic function of k_{zn}. Consequently, when the period p changes from d to L, the period of the dispersion

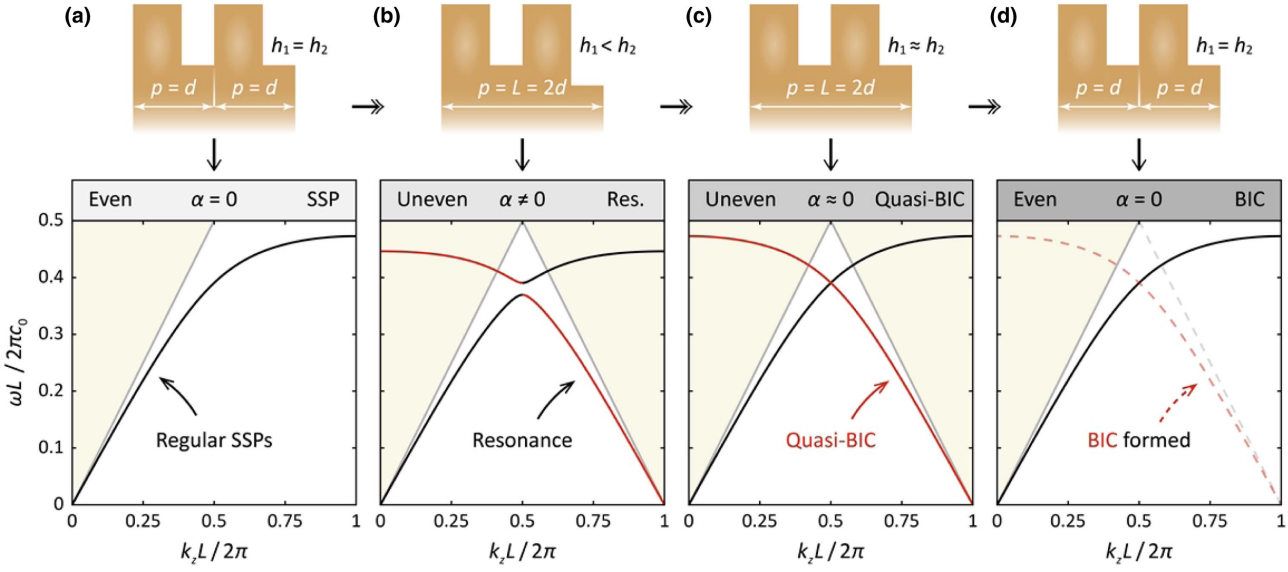

Fig. 2. Formation of SSP-based BICs induced by the asymmetry of the depth-modulated grating. When the asymmetry parameter α of the double-period grating gradually increases from zero and then gradually decreases to zero, the evolution of its dispersion relations indicates the formation process of BIC. (a) Structural illustration and dispersion of the conventional SSP when $\alpha = 0$ and $p = d$. (b) Structural illustration and folded dispersion of SSP when $\alpha \neq 0$ and $p = L$. (c) Structural illustration and folded dispersion including quasi-BIC modes when $\alpha \approx 0$ and $p = L$. (d) Structural illustration and BIC-embedded dispersion when $\alpha = 0$ and $p = d$.

curve is half of the previous one and should be collapsed and reorganized, as shown in Fig. 2(b). Compared with the symmetry one, the dispersion curve of the asymmetry grating is evolved by splitting the mode band at the boundary of the irreducible Brillouin zone ($k_z = \pi/p = \pi/L$). Since the slot depths are not the same, $h_1 < h_2$, the effective refractive indices are not the same, thereby leading to the split of the band structure at the boundary of the Brillouin zone. The split dispersion curve is also folded along the k_z axis in the ω–k_{zn} space with period $2\pi/L$. As shown in the second row of Fig. 2(b), the new space harmonic introduced due to the Brillouin-folding phenomenon is marked as red curves, which together with the black ones constitute the SSPs dispersion of the asymmetric grating. It is worth noting that a part of the spectrum of the red dispersion curve is in the fast wave region. The SSPs within this part of the spectrum are not completely localized to the surface of the grating structure but exist in a resonant state. This is because their wave vectors match those of extended modes in free space. If excited, they will propagate along the grating while radiating into free space. Therefore, these SSPs that fall within the light cone are the resonant states in the continuum of the free-space extended modes and are thus defined as resonant SSPs.

Third, when decreasing h_2 to approximately equal to h_1, i.e., $h_1 \approx h_2$ and $\alpha \approx 0$, the structural illustration and dispersion curves are shown in Fig. 3(b). Since h_2 is not exactly equal to h_1, the minimum period of the structure is still the modulation period, which yields genuine period $p = L$. Thus, the dispersion of SSP is still folded and redistributed in ω–k_{zn} space with period $2\pi/L$. However, the splitting of the dispersion curve at the boundary of the Brillouin zone is almost invisible because the two depths are almost identical. Compared to Fig. 2(a), the dispersion curve in Fig. 2(c) appears to result from a mirror symmetry of the regular SSP with $k_z = \pi/L$ as the axis. Similar to the case of $\alpha \neq 0$, due to the folding of the dispersion curve, a part of the SSP spectrum also falls into the fast wave region and can couple with the extended state to radiate into the far field. This is evident from the red solid line falling within the shaded area in Fig. 2(c). However, there is a notable difference: as demonstrated later, the SSP in the $\alpha \approx 0$ case exhibits a significantly higher Q factor and stronger field intensity than in the $\alpha \neq 0$ cases. Thus, although these partial modes are also resonances in the continuum of the extended modes, they are much more intense.

Fourth, when depth h_2 is further decreased to exactly equal to h_1, $h_1 = h_2$, and $\alpha = 0$, the asymmetric grating degenerates to the symmetric grating with the same structure as in Fig. 2(a). The genuine period should be the propagation period, $p = d$. However, if we assume that the minimum period for dispersion analysis is still the modulation period L rather than d, the calculated results are shown in Fig. 2(d). The dispersion curves of the SSPs still exhibit folding in ω–k_{zn} space with a period of π/L, except that there is no split at the boundary of the

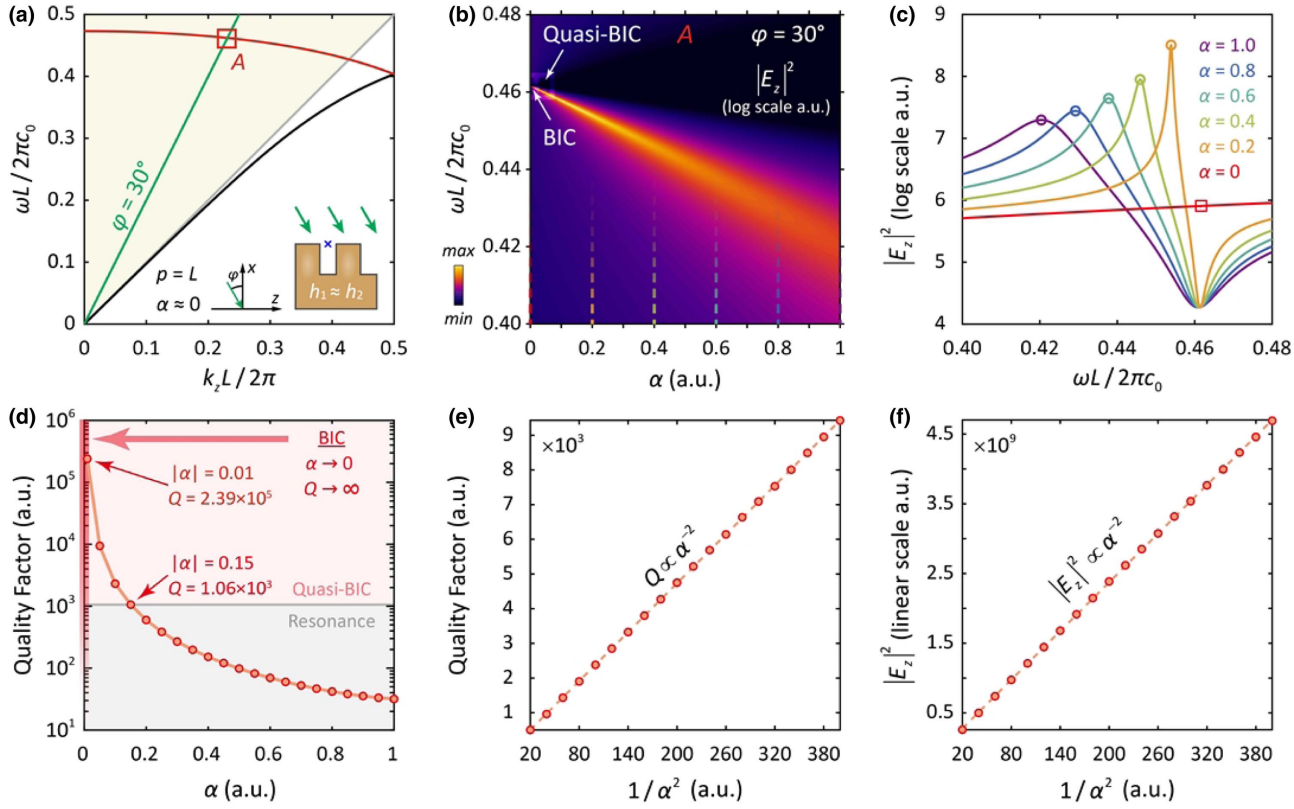

Fig. 3. Validation of symmetry-protected BIC from SSPs. (a) Dispersions of symmetry-broken grating and plane wave with incident angle $\varphi = 30°$ in the irreducible Brillouin zone, where $\alpha \approx 0$ and $p = L$. (b) Evolution of the probed spectra of $|E_z|^2$ versus asymmetry parameter α. (c) Probed spectra of $|E_z|^2$ of vertical slices in (b). (d) Dependence of the Q factor of SSP resonance on the asymmetry parameter α. (e) Linear dependence between Q factor and $1/\alpha^2$. (f) Linear dependence between the maximum of the probed intensity of $|E_z|^2$ and $1/\alpha^2$.

Brillouin zone. The new space harmonic introduced due to the Brillouin-folding phenomenon is marked as red dashed curves. Similar to the $\alpha \approx 0$ case, it appears to result from a mirror symmetry of the regular SSP with $k_z = \pi/L$ as the axis. Despite these resonant SSPs within the light cone, they cannot couple with any extended modes of free space or radiate into the far field because they do not exist when the genuine period is $p = d$ for $\alpha = 0$. Consequently, if excited, they will be confined to the surface of the grating and propagate solely along the z direction. Nonetheless, since these resonant SSPs exist within the continuum of free-space extended waves yet remain perfectly confined and free of radiation, the symmetry-protected SSP-based BICs are thus formed, exhibiting a theoretically infinite Q factor and vanishing resonant width. As depicted in Figs. 2(a) and 2(d), the proposed BICs are embedded within the dispersion of regular SSPs. However, due to symmetry protection, direct excitation or observation of these BICs is impossible in a conventional uniform grating. To break this symmetry by choosing a suitable modulation period and modulating the depths, these symmetry-protected BICs can be transformed into excitable and observable resonant modes with a limited Q factor and resonant width. Notably, the more similar the structural parameters of the symmetry-breaking structure are to those of the symmetric one, the more closely the performance of these resonant modes approaches the theoretical limit of BIC. In other words, as the asymmetry parameter α approaches zero (i.e., $\alpha \approx 0$), the resonance will exhibit a much higher Q factor and much narrower resonant width, commonly referred to as a quasi-BIC. Therefore, for the case $\alpha \approx 0$ in Fig. 2(c), the resonant SSPs falling inside the light cone are quasi-BICs, whereas the resonant one in Fig. 2(b) is not. Moreover, the proposed SSP-based BICs persist over a wide spectral range, which can be confirmed by the dispersion curve of resonant SSPs falling in the light cone. Consequently, by constructing quasi-BICs near the BICs, broadband field enhancement can be achieved to improve the efficiency of the laser or power device.

In the previous discussion, the formation process of BIC is explained only in terms of the dispersion theory. Before utilizing BIC to generate intense SPR, the validity of the proposed BIC needs to be further demonstrated from a spectral point of view. When the asymmetry parameter α is not zero, the SSPs falling in the light cone are in resonance, which can be excited by the plane waves in free space when the phase-matching conditions are met. The spectrum of this scattering investigation can be detected by placing a probe in the center of the grating slot. Then, the probed spectral information can be employed to characterize the performance of the resonance, including operating frequency, Q, and intensity. Hence, when the asymmetry parameter α decreases from one to zero, the validity of the proposed BIC could be proved by the evolution of the spectral information. To accurately describe the phase-matching between the incident plane wave and the resonant SSPs, their dispersion curves are depicted in Fig. 3(a), where the regular and resonant SSPs are marked as black and red solid lines, respectively. The green solid line indicates the TM-polarized incident wave, whose dispersion relation is $\omega_{\text{inc}} = k_{\text{inc}}c = k_0 c \sin \varphi$. The lower illustration shows the plane of incidence, where the incident angle is chosen as $\varphi = 30°$ for instance in the following analysis. The interaction point of the dispersion curves is A, implying that the resonant SSP at f_A will be excited by the incident wave. To evaluate the performance of the resonant mode, a probe is placed right in the center of the open end of the slot with depth h_1, where the simulation is performed in CST Studio Suite. Figure 3(b) shows the probed spectra while decreasing α from one to zero, illustrating the evolution of a resonance peak from weak to strong. In addition, the spectra for $\alpha = 1$, 0.8, 0.6, 0.4, 0.2, and 0 are plotted separately in Fig. 3(c) to visualize the resonance peaks of spectra. As the asymmetry parameter α decreases from one to zero, the intensity of the resonant peak becomes stronger and the resonant width becomes narrower, describing the process of BIC formation at A. As α approaches zero, the resonant width almost disappears while its intensity becomes much stronger. This behavior is a characteristic of quasi-BIC. Once $\alpha = 0$, the BIC with theoretically infinite Q is formed, while the resonant peak disappears completely in spectra due to the vanished resonant width. To better understand the formation of the symmetry-protected BIC, the resonant widths λ_δ are calculated according to $\lambda_\delta = |\lambda_{\text{peak}} - \lambda_{\text{dip}}|$, where λ_{peak} is the peak wavelength of the resonance, and λ_{dip} is the wavelength of the closest dip in the probed spectrum. The quality factors can then be evaluated by $Q = \lambda_{\text{peak}}/\lambda_\delta$ [31,39]. A direct comparison of the Q factor of resonant SSPs as functions of the asymmetry parameter α is shown in Fig. 3(d). At maximum system asymmetry, $\alpha = 1$, the Q factor of the resonance is only 31.80. However, as h_2 decreases to h_1 and α approaches zero, the Q factor increases rapidly, reaching 2.29×10^5 at $\alpha = 10^{-2}$. Therefore, as α decreases towards zero, the Q and resonant width of the resonance approach the theoretical limit of BIC. Here, the resonant SSPs with $\alpha \leq 0.15$ are referred to as quasi-BICs, as their Q factors have increased by two orders of magnitude compared with the $\alpha = 1$ case. Moreover, Figs. 3(e) and 3(f) indicate that the behavior of the Q factor and energy density of the resonant SSPs is explicitly inversely quadratic when α decreases to zero, i.e., $Q \propto |E_z|^2 \propto \alpha^{-2}$. This observation is consistent with the theoretical description of the symmetry-protected BIC presented in Ref. [40], providing further evidence for the validity of the proposed BIC.

So far, we have demonstrated the formation process of the BIC by varying the parameter α while keeping the incident angle φ fixed at 30°. As the incident angle remains constant, the resonant SSPs can only be excited at a specific frequency corresponding to a particular wavenumber $k_z \sin \varphi$. Therefore, the preceding discussion only confirms the existence of BIC in the system at a single frequency point. However, as α approaches zero, all resonant SSPs within the light cone become quasi-BICs and exhibit BIC-like behavior. Hence, it is imperative to establish the broadband presence of the resonant SSPs and the proposed BIC. First, the dispersion curves are illustrated in Fig. 4(a) for $\alpha = 0.2$, where the black and red solid curves are regular and resonant SSPs, respectively. As previously analyzed, once the phase-matching conditions are met between the incident waves and the resonances, the resonant SSPs within the fast wave region can be excited. When the incident angle φ changes, the phase-matching condition changes

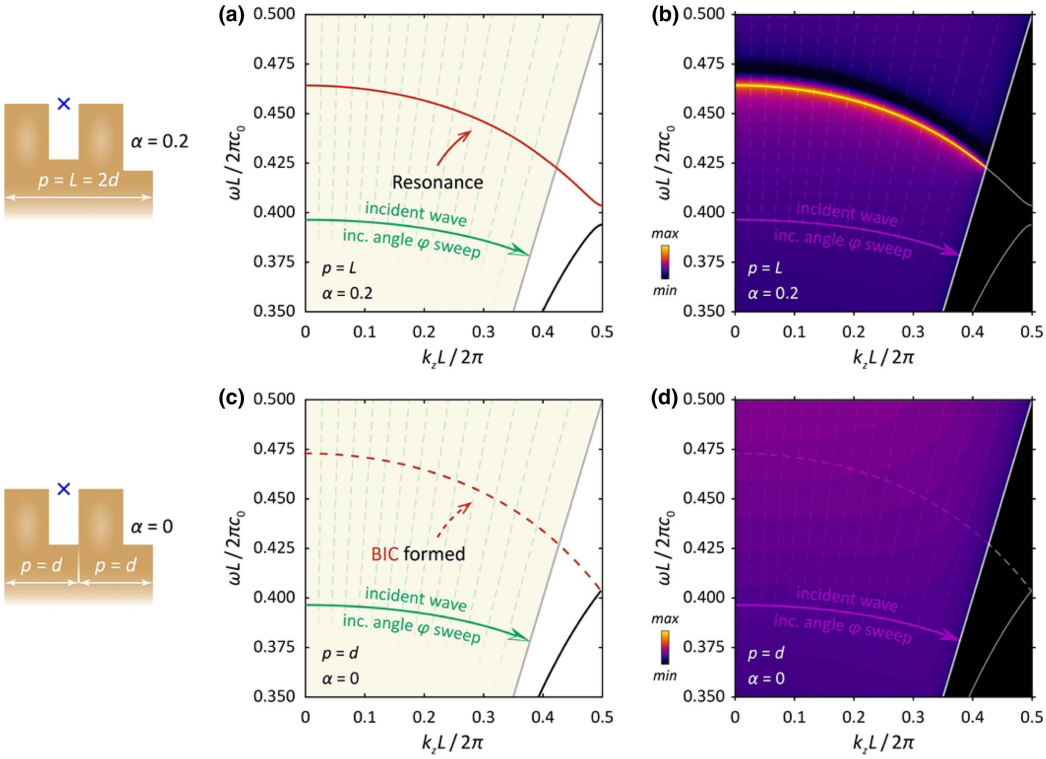

Fig. 4. Broadband presence verification for symmetry-protected BIC. (a), (c) Dispersion relations of symmetry-broken gratings when $\alpha = 0.2$ and $\alpha = 0$, respectively. (b), (d) Evolutions of the probed spectra of $|E_z|^2$ versus incident angle φ when $\alpha = 0.2$ and $\alpha = 0$, individually, where φ is remapped into wavenumber space.

accordingly due to the variation of the longitudinal wavenumber $k_{\text{inc}} = k_0 \sin \varphi$ of the incident wave. Therefore, the excitation of the SSPs at different frequencies can be achieved by altering the incident angle. When the incident angle φ gradually increases from 0° to nearly 90°, an excitation scan of resonant SSPs is achieved in the light cone, and the probed spectra are shown in Fig. 4(b). The numerical dispersion curves are also redrawn in Fig. 4(b) and marked as white solid lines. It is confirmed that the resonant peaks of the probed spectra are consistent with the theoretical dispersion curve in the light cone, thus verifying the presence of the resonant SSPs in the broadband range. As the asymmetry parameter α decreases from 0.2 to zero, the resonant SSPs first become quasi-BICs with high-Q and then turn into BICs with vanished resonant widths. The dispersion curves of resonant SSPs for $\alpha = 0$ are shown in Fig. 4(c), where the red dashed line indicates the BIC. Subsequently, the same scattering investigation is performed for the symmetry grating with $\alpha = 0$, as in the case of $\alpha = 0.2$. Figure 4(d) depicts the probed spectra, which show no resonance peaks at the positions where resonance previously existed (white dashed line). This suggests that BICs are formed in the broadband range where the resonant SSPs fall within the light cone. Therefore, it has been demonstrated that the proposed symmetry-protected BICs exist over a broad frequency range.

B. Broadband Symmetry-Protected BIC from Resonant SSPs

To further validate the hypothesis that the proposed BICs can facilitate the generation of intense SPR with strongly enhanced intensity, the simulations are performed using the Frequency Domain Solver in COMSOL, focusing on frequency-domain simulation of single-electron excitation. The radiation intensity is calculated based on the numerical model provided in Ref. [41], which presents detailed procedures for computing SPR using COMSOL or other frequency-domain numerical solvers. When the asymmetry parameter $\alpha \approx 0$, the dispersion curves are shown in Fig. 5(a), where the regular and resonant SSPs are marked as black and red solid lines. As the structural inset indicates, the 40-keV e-beam moving in the $+z$ direction is employed to excite the resonant SSPs and quasi-BICs, whose folded dispersion is illustrated as the purple solid line in Fig. 5(a). The interaction point, denoted as B, highlights the phase-matching between the SSPs and free electrons. As a result, only the resonant SSP or quasi-BIC with wavenumber k_B can be excited when the free electrons skim the grating. Since intersection B is located within the light cone, the excited high-Q quasi-BIC will be diffracted into free space, leading to the generation of the intense SPR. To illustrate the radiative nature of BIC-enhanced SPR, Fig. 5(b) shows the radiation spectra as asymmetry parameter α decreases from one to zero, in which the separate spectra of vertical slices are illustrated in Fig. 5(c). When α tends to zero, the evolution of the radiation peak from weak to strong and radiation width from wide to narrow can be observed. Figure 5(d) reveals a straight comparison of the Q factor as functions of α. The Q factor of the radiation peak is merely 28.19 for $\alpha = 1$. However, as α decreases, the Q factor increases rapidly, reaching up to 2.95×10^5 at $\alpha = 10^{-2}$.

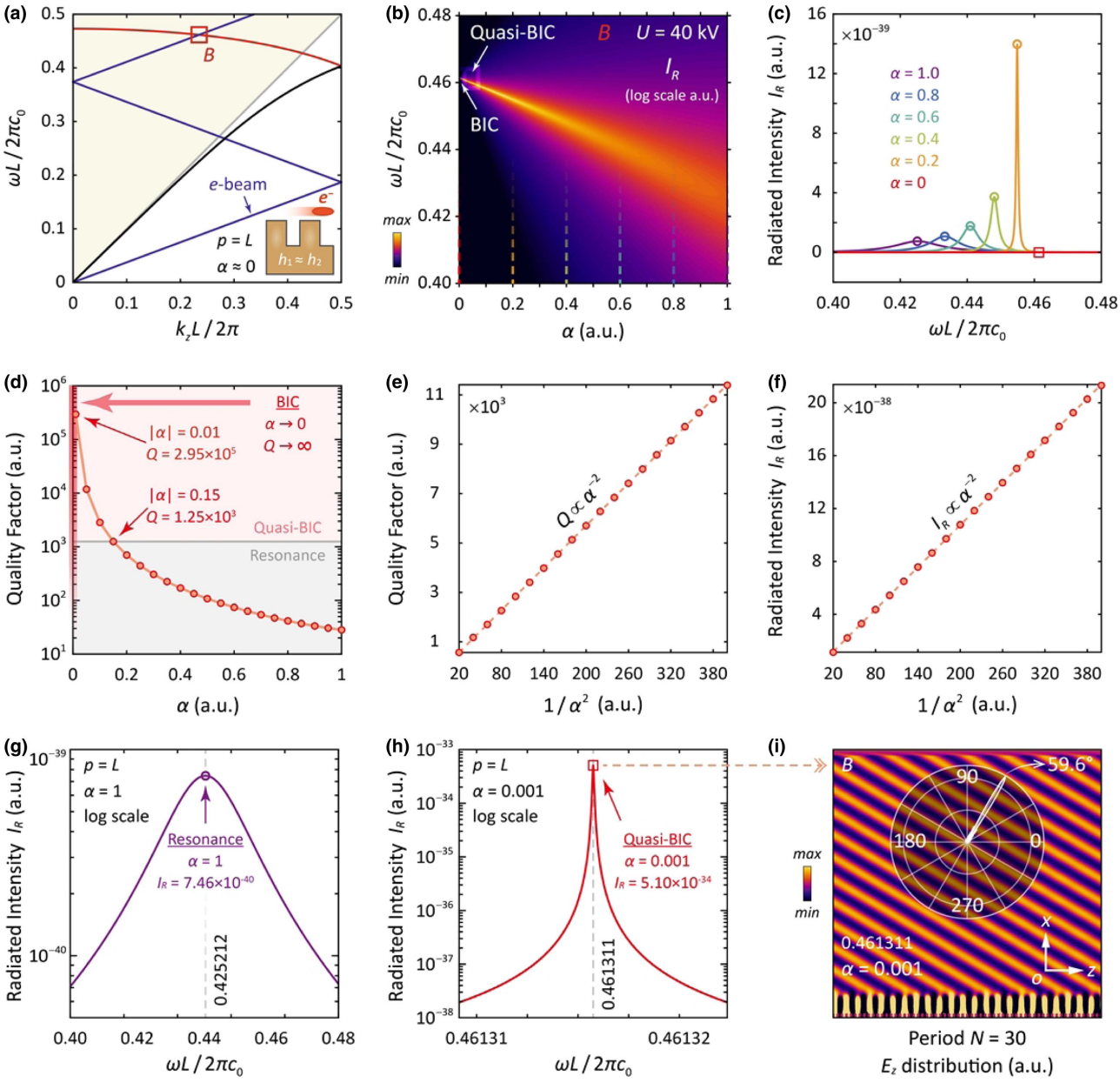

Fig. 5. Validation of intense Smith–Purcell radiation from SSP-based BIC. (a) Dispersions of symmetry-broken grating and 40-keV e-beam, where $\alpha \approx 0$ and $p = L$. (b) Evolution of the radiation intensity I_R versus asymmetry parameter α. (c) Radiation spectra of vertical slices in (b). (d) Dependence of the Q factor of radiation intensity on the asymmetry parameter α. (e) Linear dependence between the Q factor of radiation intensity and $1/\alpha^2$. (f) Linear dependence between the maximum radiation intensity of $|E_z|^2$ and $1/\alpha^2$. (g) Radiation spectra of regular Smith–Purcell radiation when $\alpha = 1$. (h) Radiation spectra of intensely enhanced Smith–Purcell radiation near the BIC when $\alpha = 0.001$. (i) Field distribution and far-field directivity of the strongest radiation point in (h).

Once $\alpha = 0$, a BIC with theoretically infinite Q is formed. Since its resonant width vanishes, the resulting intense SPR cannot be observed in the radiation spectrum.

Moreover, Figs. 5(e) and 5(f) indicate that the behaviors of the Q factor and radiation intensity I_R of the intense SPR are both inverse quadratics when α decreases to zero, i.e., $Q \propto I_R \propto \alpha^{-2}$. Therefore, as α approaches zero, the Q factor of the resonant SSP becomes higher, resulting in enhanced radiation intensity. These findings align with the BIC formation results presented in Fig. 3 and provide further evidence that the high-Q quasi-BICs can enhance the intensity of SPR. In addition, to evaluate enhancement performance, the spectra of regular and intense radiations corresponding to $\alpha = 1$ and 10^{-3} are shown in Figs. 5(g) and 5(h), respectively. At $\alpha = 1$, the resulting SPR is coherent with a low-Q resonant SSP, which only produces a peak radiation intensity of 7.46×10^{-40}. However, as α decreases towards zero, the low-Q resonant SSP gradually transitions to the high-Q quasi-BIC. At $\alpha = 10^{-3}$, the peak radiation intensity from this quasi-BIC is 5.10×10^{-34}, which is six orders of magnitude higher than $\alpha = 1$.

This significant enhancement clearly demonstrates the potential of leveraging high-Q quasi-BICs for boosting SPR radiation intensity. In addition to this, Fig. 5(i) shows the E_z distribution and the far-field directivity at the frequency of the radiation peak for $\alpha = 10^{-3}$. The angle between the radiation direction and the $+z$ direction is 59.6°. This is consistent with the prediction of the Smith–Purcell relation [1],

$$\theta = \arccos\left(\frac{c}{v_e} - \frac{c}{f}\frac{|n|}{L}\right), \tag{6}$$

where θ is the defined radiation angle, and v_e is the electron velocity.

As previously proved, the proposed BICs exist over a broad frequency range where the resonant SSPs reside in the light cone. Consequently, it is expected that the intense SPR will be emitted over this entire broadband spectrum. However, the excitation through a single voltage ($U = 40$ kV) e-beam only reveals that the intense SPR can be generated at a specific frequency point corresponding to the wavenumber k_B. To further confirm its broadband radiation capability based on BIC, it is crucial to vary the voltage U and examine the resulting radiation spectral and angular distribution. When $\alpha = 0.01$, dispersion curves are redrawn in Fig. 6(a), where the regular and resonant high-Q SSPs are marked as black and red solid lines. As voltage U decreases from 83 kV to 14 kV, the dispersions of the corresponding e-beams are shown by the purple dashed lines, which sweep over the region where the quasi-BIC exists. Thus, based on the elaborately selected operation voltage, all high-Q quasi-BICs can be excited to generate the intense SPR with broadband tunability. In Fig. 6(b), the radiation spectra of the intense SPR are presented, and the corresponding numerical dispersion curves are also redrawn and indicated as white solid lines. The coincidence of the radiation peaks with the theoretical dispersion in the light cone confirms the successful excitation of intense SPR over a wide range of frequencies. Moreover, Fig. 6(c) illustrates the change in radiation spectra with respect to the radiation angle θ as the voltage U is changed. The results indicate that the radiation angle spans from 0° to nearly 90°, and the beam scanning of the intense SPR can be achieved by adjusting the electron voltage.

3. EXPERIMENTS AND DISCUSSION

So far, the 2D plasmonic grating is employed to construct the symmetry-protected BIC based on the resonant SSPs. However, this approach to constructing BICs is not limited to 2D gratings but can also be implemented for other plasmonic or guided-wave systems. For instance, as illustrated by the unit cell in Fig. 7(a), a realistic 3D ultrathin plasmonic grating (with thickness tending to zero in the y direction) has dispersion relations and propagation characteristics similar to those of the SSPs in the 2D scheme [42,43]. In the following, the existence of symmetry-protected BIC is demonstrated theoretically and experimentally based on this ultrathin grating. The in-plane structural descriptions remain consistent with the 2D configuration illustrated in Fig. 1, with the sole distinction being that the 2D grating is mirrored along the z axis, resulting in a bilateral grating. The thickness of the metallic grating in the y direction is $g_m = 0.007d$, and the relative permittivity and thickness of the dielectric substrate are chosen as $\varepsilon_r = 3.48$ and $g_s = 0.1d$, respectively. By employing the Eigenmode Solver in CST Studio Suite, the corresponding dispersion curves of SSPs are depicted in Fig. 7(b), taking the asymmetry parameter $\alpha \approx 0$ as an example. Identical to the dispersion curves in Fig. 3(b), the ultrathin grating has both regular and resonant SSPs, where the resonant SSPs within the light cone can be excited by the extended waves in free space. As illustrated in Fig. 7(a), two ports of the scattering investigation are the two faces of the unit cell perpendicular to the y direction. Therefore, when a plane wave impinges on the ultrathin grating, the corresponding resonant SSP should be excited through the phase-matching. Then, the spectra of the S21 parameters or the scattering efficiency on Port 1 can be employed to differentiate the resonance, including its resonant width and resonant frequency. As the asymmetry parameter α decreases from one to zero, the formation of the proposed BIC is observable through the evolution of the spectrum. To facilitate the description of the phase-matching between the incident wave and the SSPs, the dispersion curve of the incident TM-polarized plane wave is illustrated as the green solid line in Fig. 7(b), where the incident angle $\varphi = 0°$. Since the interaction point of the dispersion curves is C, the resonant SSPs in the light cone can be excited by the incident wave

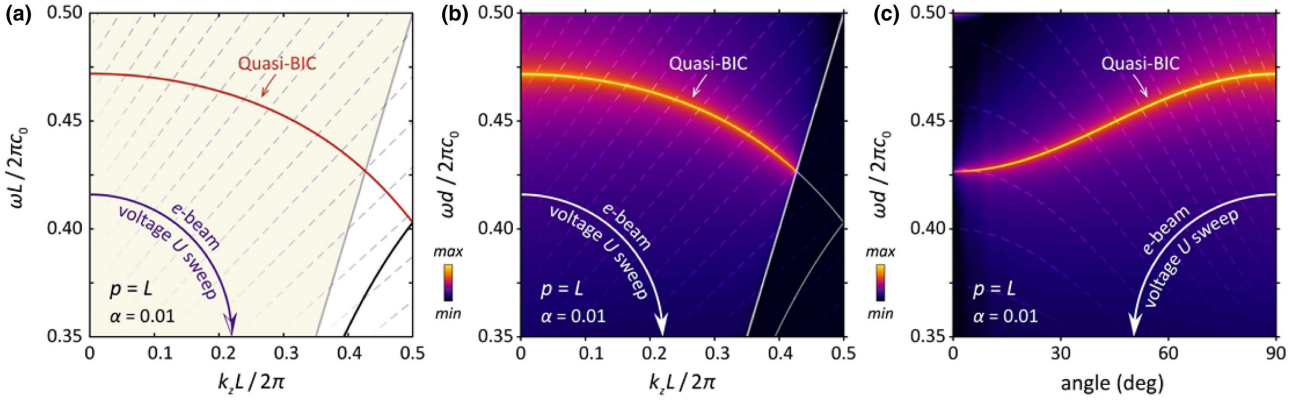

Fig. 6. Broadband enhancement verification for intense Smith–Purcell radiation from SSP-based BICs. (a) Dispersion relations of symmetry-broken gratings and e-beams when $\alpha = 0.01$. (b) Evolutions of the radiation spectra versus voltage U of e-beams, where U is remapped into wavenumber space. (c) Evolutions of radiation spectra versus radiation angles as voltage U alters.

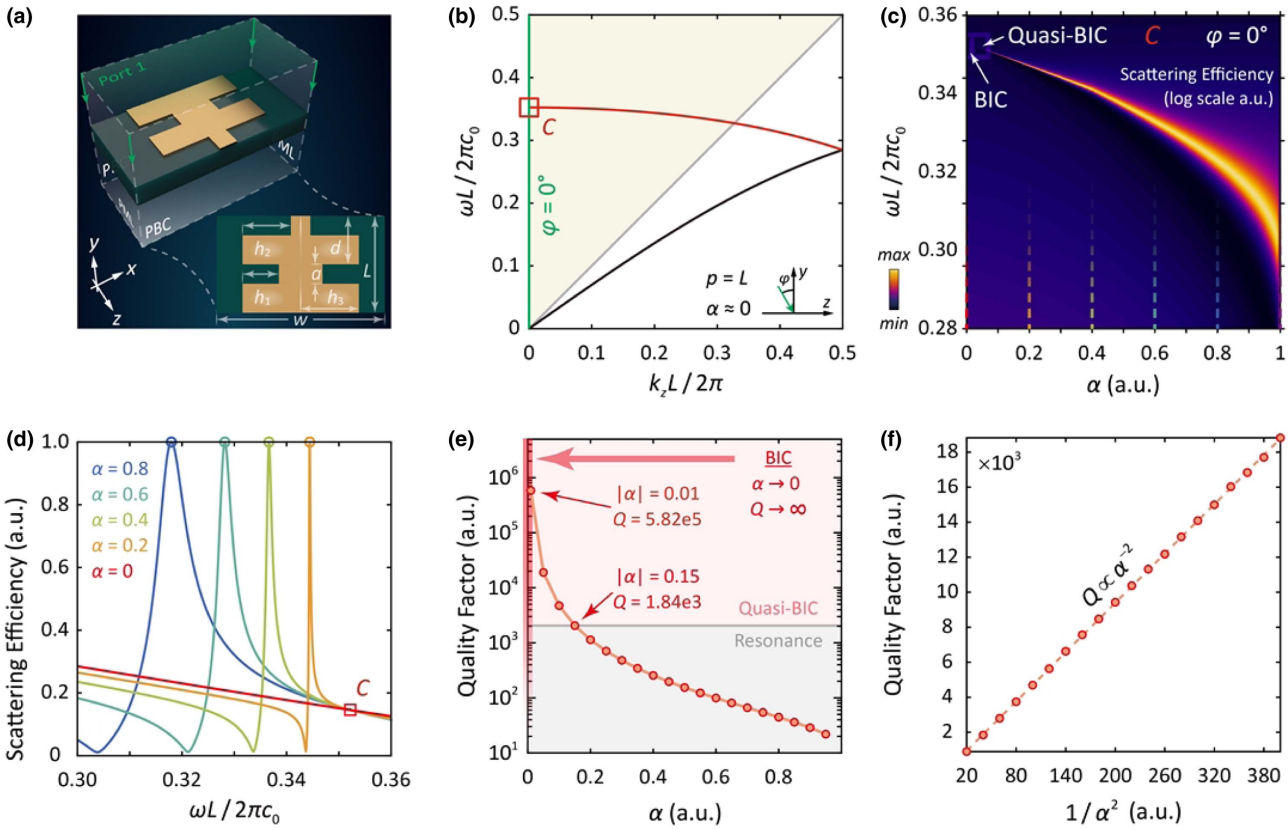

Fig. 7. Demonstration for SSP-based BIC from ultrathin plasmonic metasurface. (a) Schematic drawing of the unit cell of the ultrathin plasmonic metasurface (periodic in z). (b) Dispersions of symmetry-broken ultrathin plasmonic metasurface and plane wave with incident angle $\varphi = 0°$, where $\alpha \approx 0$ and $p = L$. (c) Evolution of the reflection spectra (zero-order diffraction) versus asymmetry parameter α. (d) Reflection spectra of vertical slices in (c). (e) Dependence of the Q factor of the resonance of ultrathin plasmonic metasurface on the asymmetry parameter α. (f) Linear dependence between the Q factor of the resonance of ultrathin plasmonic metasurface and $1/\alpha^2$.

at frequency f_C, which can be then confirmed by the resonant peak. To visualize the BIC formation based on the resonant SSP of an ultrathin grating, Fig. 7(c) shows the spectra of scattering efficiency as α decreases from one to zero, where its vertical slices are separately depicted in Fig. 7(d). Similar to the previous observations, the resonant peak grows strong and the resonant width gets narrow as α tends to zero. Once $\alpha = 0$, the resonant SSP becomes BIC along with a vanished resonant peak in scattering efficiency. Figure 7(e) gives a comparison between the Q factor and the asymmetry parameter α, indicating that the Q factor increases rapidly as α approaches zero. Figure 7(f) denotes that the behavior of the Q factor is also inversely quadratic when α decreases to zero, i.e., $Q \propto \alpha^{-2}$. This deduction is in harmony with the nature of the symmetry-protected BIC, thereby validating the formation of the BIC.

The ultrathin plasmonic grating can be easily fabricated on printed circuit board laminates, making it feasible to experimentally verify the SSP-based BIC using plasmonic antennas based on the ultrathin grating. When $\alpha \neq 0$, the grating supports resonant SSPs with a limited Q factor and resonant width. Once these resonant SSPs are excited, they radiate into free space and the device behaves as an antenna, resulting in a distinct resonance in the far-field spectrum. However, as $\alpha = 0$, the resonant SSPs become BIC with an infinite Q factor. The resonant width of the BIC vanishes, causing resonant peaks to become unobservable in the far-field spectrum. Thus, the transformation of SSPs from resonance to BIC can be validated by comparing the far-field spectra of two plasmonic antennas with $\alpha = 0$ and $\alpha \neq 0$. Specifically, the presence of the resonance in the far-field spectrum corresponds to resonant SSPs, while the absence of the resonance corresponds to the BIC.

We conducted experiments in the microwave regime using two fabricated plasmonic antennas, one with $\alpha = 0$ and the other with $\alpha = 0.4$. As shown in Fig. 8, the plasmonic antennas are fabricated using printed circuit board technology, where Rogers RO4350B with a relative permittivity of $\varepsilon_r = 3.48$ is selected as the substrate material, and the thickness of the substrate is $g_s = 0.508$ mm with an outer copper thickness of $g_m = 0.035$ mm. Since the wavenumbers of the regular SSPs supported by the ultrathin grating are larger than those of free space, it is hard to directly excite and extract the spectral information of SSPs. To overcome this difficulty, the method that bridges the mismatch between the conventional coplanar waveguide (CPW) and the ultrathin grating of Ref. [42] is employed in this work. As shown in Fig. 9(a), the depth-modulated ultrathin grating is launched via two CPWs with 50 Ω impedance, which can be excited directly by a transmission line

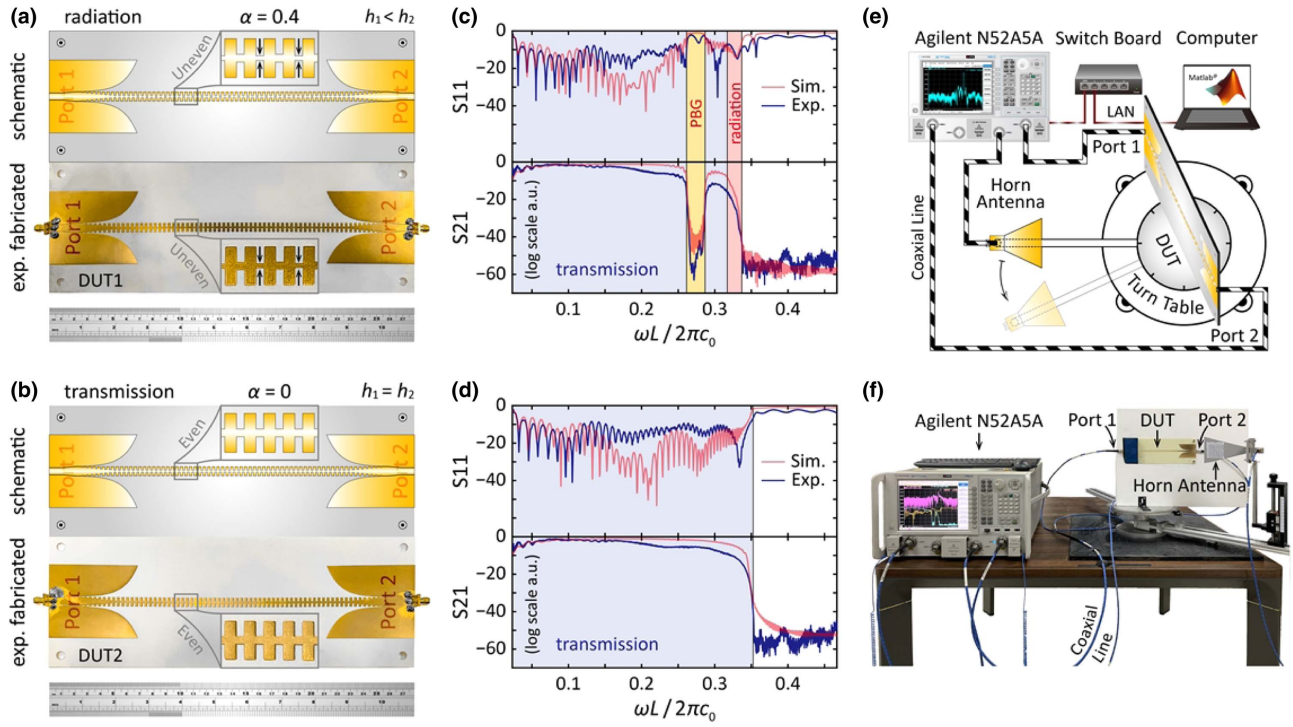

Fig. 8. Experimental setups and verification. (a), (b) Plasmonic antennas fabricated in the microwave band with $\alpha = 0.4$ and $\alpha = 0$, respectively. (c), (d) Measured and simulated S parameters of the plasmonic antennas when $\alpha = 0.4$ and $\alpha = 0$, respectively. (e) Experimental setup for testing the plasmonic antennas. (f) Real experimental setup corresponding to (e).

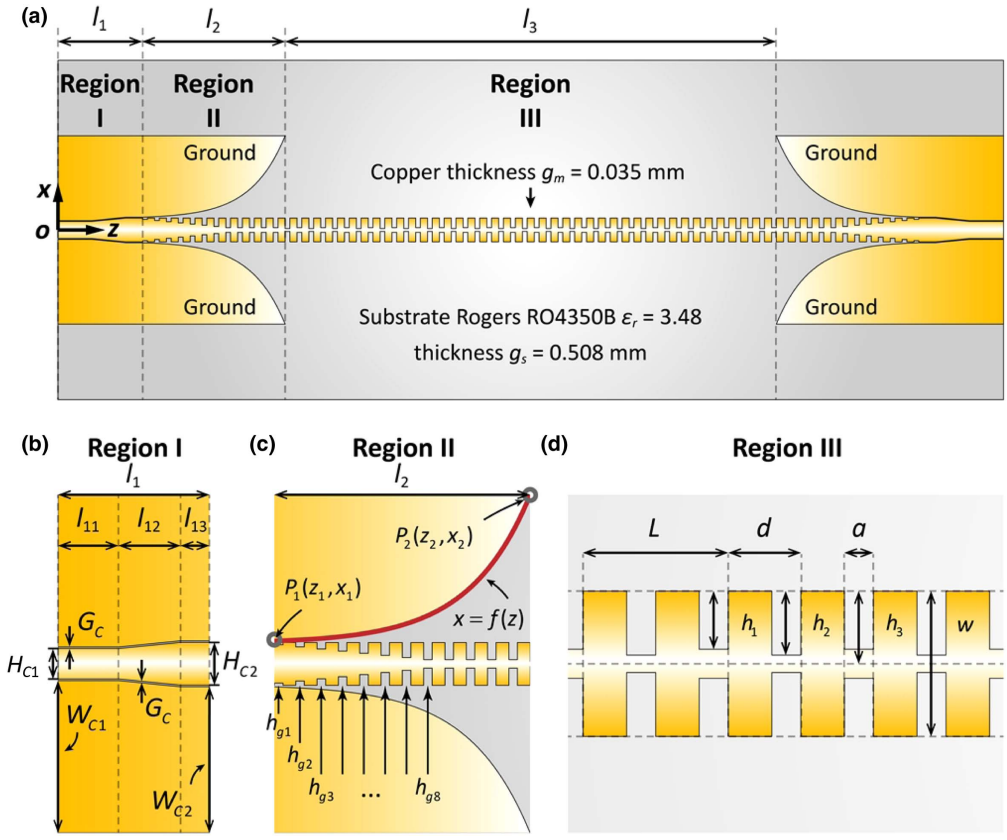

Fig. 9. Illustration and structural description of the plasmonic antenna. (a) Hybrid CPW-SSP plasmonic antenna. (b) Segment of CPW, where the inner conductor is narrow to wide for phase compensation. (c) Matching transition with gradient grooves and flaring ground. (d) Ultrathin plasmonic grating with modulated depths.

connected to the SMA interface on the vector network. The whole structure is divided into three regions, as indicated by regions I, II, and III in Fig. 9. Region I is the CPW segment, which consists of CPWs with two widths of the inner conductor and a gradient segment. The width of the inner conductor of the CPW is increased from H_{C1} to H_{C2} by a gradient segment to ensure that the grating can operate in the band that can be measured under our existing experimental conditions (8.2–18 GHz) when its proportion is the same as the discussion in the main text. Moreover, the proposed CPW segment supports the TEM mode with free-space wavenumber k_0. To guarantee that the impedance of CPW is 50 Ω, the dimensions of CPW are optimized as $H_{C1} = 5$ mm, $H_{C2} = 7$ mm, $W_{C1} = 25$ mm, $W_{C2} = 24$ mm, and $G_C = 0.26$ mm, where the lengths of these parts are $l_{11} = 10$ mm, $l_{12} = 10$ mm, $l_{13} = 5$ mm, and $l_1 = l_{11} + l_{12} + l_{13} = 25$ mm. Region III is the proposed ultrathin plasmonic grating for demonstrating the formation of the symmetry-protected BIC. The propagation and modulation periods, width, two modulated depths, and the thicknesses of the single-side and double-side grating are $d = 3.5$ mm, $L = 2d = 7$ mm, $a = 1.4$ mm, $h_1 = 2.8$ mm, $w = 7$ mm, and $h_3 = 2.8$ mm when asymmetry parameter $\alpha = 0$ and 3.08 mm when $\alpha = 0.4$.

Due to the phase-mismatch between the CPW and ultrathin grating, the TEM mode of the CPW cannot be directly transformed into SSPs with large longitudinal wavenumbers. To match the wavenumber of the CPW to the plasmonic grating, a transition is proposed and shown in Fig. 9(c). This transition consists of a flaring ground and gradient slots, where the slot depth increases from $h_{g1} = 0.35$ mm to $h_{g8} = 2.8$ mm with a step of 0.35 mm. The profile of the flaring ground that is marked as red can be described as

$$x = f(z) = C_1 e^{\zeta z} + C_2, \quad z_1 < z < z_2, \tag{7}$$

where the coefficients are $C_1 = (x_2 - x_1)/(e^{\zeta z_2} - e^{\zeta z_1})$, $C_2 = (x_1 e^{\zeta z_2} - x_2 e^{\zeta z_1})/(e^{\zeta z_2} - e^{\zeta z_1})$, and $\zeta = 0.1$. The coordinates $P_1 = (z_1, x_1) = (25, 3.76)$ and $P_2 = (z_2, x_2) = (67, 27.76)$ are the start and end points of the profile. Moreover, along with the gradient slots, they are employed to compensate for the mismatch of the longitudinal wavenumber between the CPW and plasmonic grating. As transmitted through the transition section, the wavenumber and impedance of the guided mode of CPW match those of the SSPs. Hence, the resonant SSP can be effectively excited by the input signal of CPWs, thereby facilitating the verification of the formation of the symmetry-protected BIC by distinguishing the resonance of the far-field spectra.

Figures 8(a) and 8(c) show the fabricated antennas, while Figs. 10(a) and 10(b) depict their dispersion curves for $\alpha = 0.4$ and $\alpha = 0$, respectively. Performing scattering investigations similar to Figs. 4 and 6, the scattering spectra are shown in Figs. 10(c) and 10(d), respectively, and their corresponding dispersion curves are represented by white lines. For $\alpha = 0.4$, a series of clear resonant peaks belonging to the

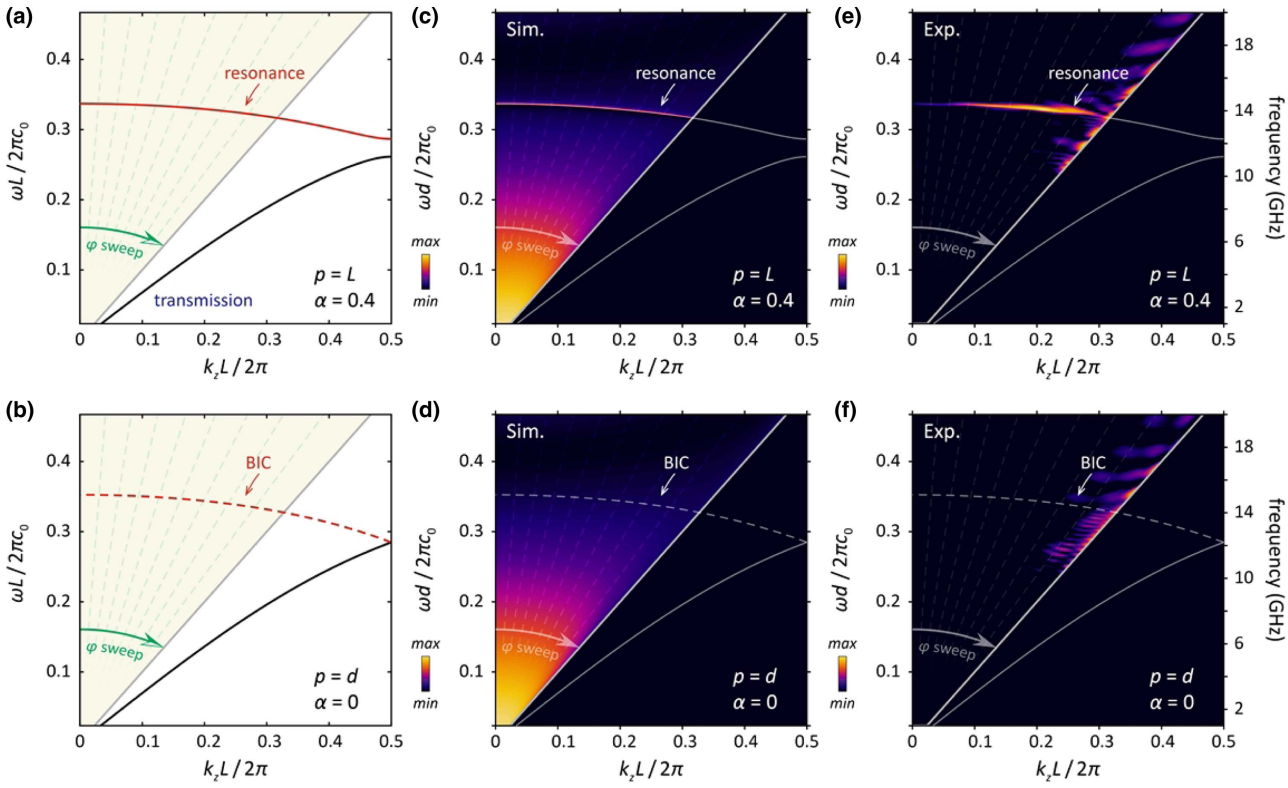

Fig. 10. Theoretical and experimental results of plasmonic antenna. (a), (b) Dispersion relations of ultrathin plasmonic metasurface when $\alpha = 0.4$ and $\alpha = 0$, respectively. (c), (d) Simulated evolutions of the reflection spectra versus incident angle φ when $\alpha = 0.4$ and $\alpha = 0$, respectively, where φ is remapped into wavenumber space. (e), (f) Measured evolutions of the S21 spectra versus radiation angle θ when $\alpha = 0.4$ and $\alpha = 0$, respectively, where θ is remapped into wavenumber space.

resonant SSPs can be observed inside the light cone, perfectly overlapping with the dispersion curve. As α approaches zero, the resonant peaks in the far-field spectrum disappear, indicating the reduction of the resonant width to zero and the formation of a BIC. Therefore, the appearance and disappearance of the resonant peaks in the far-field radiation spectrum correspond to the transition of SSPs from resonances to BICs. To carry out experiments for exciting the resonant SSPs and extracting the radiation spectrum, the schematic and realistic experimental setups for testing the antennas are shown in Figs. 8(e) and 8(f). These setups consist of an Agilent N5245A PNA-X network analyzer (10 MHz–50 GHz), a horn antenna to extract the radiation signal from resonant SSPs, a turntable to receive signals in different directions, a computer and a switch broad to program the PNA, and the device under test (DUT). Three ports of the PNA are utilized for testing, with one port connected to Port 1 of the plasmonic antenna for excitation of the SSP, while the other two are connected to Port 2 and the horn antenna for receiving S21 and extracting the far-field spectrum, respectively.

At $\alpha = 0.4$, both simulated and experimental results of the reflection parameter S11 and transmission coefficient S21 from Port 1 to Port 2 are shown in Fig. 8(c), with the two results being in good agreement. The S parameter in the blue region indicates that the SSPs, which are converted from the CPW modes at Port 1, can be transmitted through the ultrathin grating to the other end. Hence, the effectiveness of the designed structure in exciting SSPs is demonstrated. However, there is a significant drop in transmission performance in two normalized frequency ranges, 0.261 to 0.286 and 0.317 to 0.336, as indicated by the dark yellow and red-shaded regions. As shown in Fig. 10(a), the decrease in transmission performance in the dark yellow region is attributed to the photonic bandgap (PBG) between the resonant SSPs and the regular SSPs, while in the red region, it is caused by the radiation of the resonant SSPs to free space. The far-field radiation spectra detected by the horn antenna are shown in Fig. 10(e). Similar to the simulated spectrum in Fig. 10(c), a series of obvious resonance peaks belonging to the resonant SSPs are present in the frequency range of 0.317 to 0.336, demonstrating that the resonant SSPs exist in the broadband range. The presence of these resonance peaks is consistent with the dispersion curves and confirms that the designed antenna can effectively excite regular and resonant SSPs with good transmission and radiation performance.

However, at $\alpha = 0$, the measured S parameters depicted in Fig. 8(d) show no decrease in energy transmission from Port 1 to Port 2 for frequencies below 0.352. As the frequency is greater than 0.352, the energy from Port 1 is completely reflected. This can be explained by the dispersions shown in Fig. 10(b). The regular SSPs supported by the ultrathin grating have a maximum frequency of 0.352, below which the SSPs converted from the CPW modes of Port 1 can be transmitted from one end of the ultrathin grating to the other. Nonetheless, for frequencies higher than this, the CPW mode of Port 1 cannot be transmitted to Port 2 and is completely reflected due to the lack of matching modes. For frequencies below 0.352, good transmission means that no radiation is generated by the antenna. In other words, the resonant widths of the resonant SSPs vanish. The far-field radiation spectra detected by the horn antenna are shown in Fig. 10(d). The resonant peaks, which are initially observable for the spectrum of the resonant SSPs, become imperceptible, similar to the simulation results depicted in Fig. 10(c). This implies that the SSPs transition from resonances to BICs with vanished resonant widths. In summary, the existence of symmetry-protected BICs based on ultrathin gratings has been demonstrated through two sets of plasmonic antennas with different symmetry factors, and their formation process has been verified over a wide frequency range. It is noteworthy that in this experiment, the plasmonic antennas are merely carriers used to demonstrate the existence of the BIC. Such a symmetry-protected BIC has always existed in periodic systems, such as plasmonic systems, guided-mode systems, photonic crystals, and metasurfaces. However, their effective extraction and utilization have been a challenge. Recently, a double-band-folding strategy to achieve high-Q leaky modes in compound lattices demonstrated that the Q factor of these leaky modes can be made ultrahigh at any incident angle [44]. Likewise, an approach to achieve sustainable ultrahigh Q factors by engineering Brillouin-zone-folding-induced BICs (BZF-BICs) is proposed, providing a unique design path for robust silicon metasurface cavities with extreme Q factor enhancement throughout a large, tunable momentum space [45]. The SSP-based BICs proposed in this work share similarities with those in Refs. [44,45], all falling under the category of BZF-BICs, which are characterized by a folded-dispersion curve of resonance in momentum space. For SSP-based BICs with $h_1 = h_2 \ll d$ and $\alpha = 0$, the periodic modulation acts as a small perturbation, leading to folded bands exhibiting infinitely high radiative Q factors. Additionally, by adjusting the propagation period d in this scenario with $\alpha \approx 0$, it is possible to achieve a broadband quasi-BIC covering a large range of ω–k space. As for conventional plasmonic leaky wave antennas, they operate first by exciting the resonant SSPs and then radiating them into the far field. By appropriately adjusting the structural parameters, the corresponding asymmetric factors can be minimized, facilitating the construction of a similar symmetry-protected BIC [44].

In the above analysis, we choose two propagation periods as one modulation period, and the slot depths are modulated to break the symmetry of the grating. This enables us to construct a symmetry-protected BIC in a broadband range, resulting in enhanced SPR across a wide spectrum, as depicted by the red-shaded area in Fig. 11(a). One can increase the number of propagation periods within one modulation period to expand the frequency range available for enhanced radiation. For example, when considering three propagation periods within one modulation period, the dispersion curves are shown in Fig. 11(b). As a result of the increased modulation period, the Brillouin zone boundary moves closer to the origin. Based on the Brillouin-folding phenomenon, a greater portion of the folded plasmonic dispersion curve falls within the light cone, further expanding the frequency range for the available BIC. The larger red-shaded area confirms this expansion in Fig. 11(b) compared to Fig. 11(a). Similarly, increasing the number of propagation periods within the modulation period can further increase the proportion of folded dispersion that

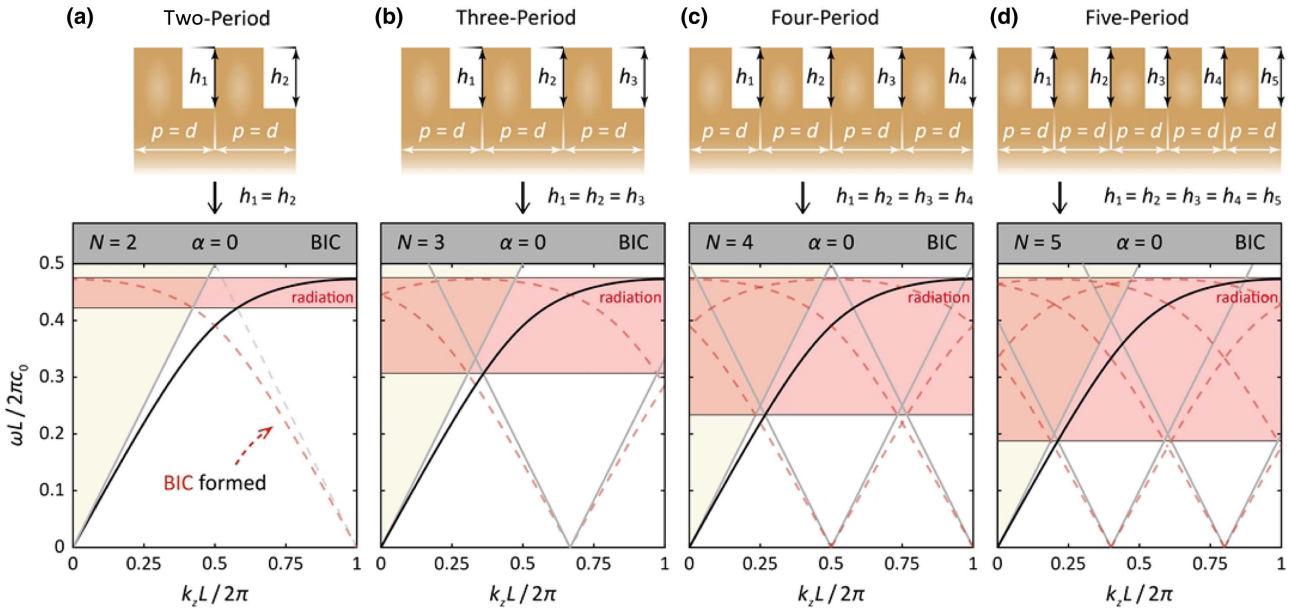

Fig. 11. Dispersion curves of SSPs under different modulation periods. The dispersion curves and BIC distribution of SSPs with two, three, four, and five propagation periods within one modulation period are shown in (a), (b), (c), and (d), respectively. The solid black lines represent conventional SSPs, while the dashed red lines represent BIC modes resulting from resonant SSPs' transformation.

falls within the light cone, thereby expanding the frequency range of BIC that can be used to achieve enhanced radiation, as shown by the increased red-shaded areas in Figs. 11(c) and 11(d). Therefore, by selecting different modulation periods, one can selectively expand the spectral range in which this symmetry-protected BIC exists.

4. CONCLUSION

In conclusion, this study proposes and experimentally validates the symmetry-protected BICs that operate over a broad spectral range and achieve intense SPR using quasi-BICs. By breaking the symmetry of the double-slot plasmonic grating, a symmetry-protected BIC is constructed based on the SSPs, and the evolution from resonance to BIC is presented. The proposed BIC is then employed to enable tunable intense SPR in broadband, with a theoretical increase in radiation intensity of six orders of magnitude compared to conventional SPR that is coherent with regular SSPs. Notably, the methodology for constructing BIC is not limited to 2D gratings but can be extended to other plasmonic or guided-mode systems. Two plasmonic antennas are fabricated in the microwave regime based on an ultrathin scheme to demonstrate the formation of BICs in theory and experiment. Given the rapid advances in nanophotonics, the proposed intense SPR has the potential to pave the way for compact free-electron sources in the terahertz and far-infrared bands.

Funding. National Natural Science Foundation of China (62271011, U21A20458); National Key Research and Development Program of China (2021YFA1600302); Beijing Science Foundation for Distinguished Young Scholars (JQ21011).

Acknowledgment. The authors acknowledge discussions with Fan-Hong Li, Mian Wang, and Chong-Qi Zhang.

Disclosures. The authors declare no conflicts of interest.

Data Availability. The data that support the findings of this study are available from the corresponding author upon reasonable request.

REFERENCES

1. S. J. Smith and E. M. Purcell, "Visible light from localized surface charges moving across a grating," Phys. Rev. **92**, 1069 (1953).
2. G. Doucas, V. Blackmore, B. Ottewell, C. Perry, P. G. Huggard, E. Castro-Camus, M. B. Johnston, J. L. Hughes, M. F. Kimmitt, B. Redlich, and A. van der Meer, "Longitudinal electron bunch profile diagnostics at 45 MeV using coherent Smith-Purcell radiation," Phys. Rev. Spec. Top. Accel. Beams **9**, 092801 (2006).
3. L. Schächter and A. Ron, "Smith-Purcell free-electron laser," Phys. Rev. A **40**, 876–896 (1989).
4. Y. Yang, C. Roques-Carmes, S. E. Kooi, H. Tang, J. Beroz, E. Mazur, I. Kaminer, J. D. Joannopoulos, and M. Soljačić, "Photonic flatband resonances for free-electron radiation," Nature **613**, 42–47 (2023).
5. Y. Yang, A. Massuda, C. Roques-Carmes, S. E. Kooi, T. Christensen, S. G. Johnson, J. D. Joannopoulos, O. D. Miller, I. Kaminer, and M. Soljačić, "Maximal spontaneous photon emission and energy loss from free electrons," Nat. Phys. **14**, 894–899 (2018).
6. S. L. Chuang and J. A. Kong, "Enhancement of Smith–Purcell radiation from a grating with surface-plasmon excitation," J. Opt. Soc. Am. A **1**, 672–676 (1984).
7. Z. Su, B. Xiong, Y. Xu, Z. Cai, J. Yin, R. Peng, and Y. Liu, "Manipulating Cherenkov radiation and Smith–Purcell radiation by artificial structures," Adv. Opt. Mater. **7**, 1801666 (2019).
8. Z. Wang, K. Yao, M. Chen, H. Chen, and Y. Liu, "Manipulating Smith-Purcell emission with Babinet metasurfaces," Phys. Rev. Lett. **117**, 157401 (2016).

9. Z. Su, F. Cheng, L. Li, and Y. Liu, "Complete control of Smith-Purcell radiation by graphene metasurfaces," ACS Photon. **6**, 1947–1954 (2019).
10. L. Jing, X. Lin, Z. Wang, I. Kaminer, H. Hu, E. Li, Y. Liu, M. Chen, B. Zhang, and H. Chen, "Polarization shaping of free-electron radiation by gradient bianisotropic metasurfaces," Laser Photon. Rev. **15**, 2000426 (2021).
11. J.-F. Zhu, C.-H. Du, Z.-W. Zhang, P.-K. Liu, L. Zhang, and A. W. Cross, "Smith–Purcell radiation from helical grating to generate wideband vortex beams," Opt. Lett. **46**, 4682–4685 (2021).
12. L. Jing, Z. Wang, X. Lin, B. Zheng, S. Xu, L. Shen, Y. Yang, F. Gao, M. Chen, and H. Chen, "Spiral field generation in Smith-Purcell radiation by helical metagratings," Research **2019**, 3806132 (2019).
13. Z.-W. Zhang, J.-F. Zhu, C.-H. Du, F. Gao, F.-Y. Han, and P.-K. Liu, "Chiral plasmons enable coherent vortex Smith–Purcell radiation," Laser Photon. Rev. **17**, 2200420 (2023).
14. M. Wang, F. Liu, Y. Lin, K. Cui, X. Feng, W. Zhang, and Y. Huang, "Vortex Smith-Purcell radiation generation with holographic grating," Photon. Res. **8**, 1309–1315 (2020).
15. R. Remez, N. Shapira, C. Roques-Carmes, R. Tirole, Y. Yang, Y. Lereah, M. Soljačić, I. Kaminer, and A. Arie, "Spectral and spatial shaping of Smith-Purcell radiation," Phys. Rev. A **96**, 061801 (2017).
16. J. R. M. Saavedra, D. Castells-Graells, and F. J. García de Abajo, "Smith-Purcell radiation emission in aperiodic arrays," Phys. Rev. B **94**, 035418 (2016).
17. A. Karnieli, D. Roitman, M. Liebtrau, S. Tsesses, N. Van Nielen, I. Kaminer, A. Arie, and A. Polman, "Cylindrical metalens for generation and focusing of free-electron radiation," Nano Lett. **22**, 5641–5650 (2022).
18. Y.-C. Lai, T. C. Kuang, B. H. Cheng, Y.-C. Lan, and D. P. Tsai, "Generation of convergent light beams by using surface plasmon locked Smith-Purcell radiation," Sci. Rep. **7**, 11096 (2017).
19. S. Liu, C. Zhang, M. Hu, X. Chen, P. Zhang, S. Gong, T. Zhao, and R. Zhong, "Coherent and tunable terahertz radiation from graphene surface plasmon polaritons excited by an electron beam," Appl. Phys. Lett. **104**, 201104 (2014).
20. S. Liu, P. Zhang, W. Liu, S. Gong, R. Zhong, Y. Zhang, and M. Hu, "Surface polariton Cherenkov light radiation source," Phys. Rev. Lett. **109**, 153902 (2012).
21. H. Hu, X. Lin, D. Liu, H. Chen, B. Zhang, and Y. Luo, "Broadband enhancement of Cherenkov radiation using dispersionless plasmons," Adv. Sci. **9**, 2200538 (2022).
22. J.-F. Zhu, C.-H. Du, L.-Y. Bao, and P.-K. Liu, "Regenerated amplification of terahertz spoof surface plasmon radiation," New J. Phys. **21**, 033021 (2019).
23. D. Zhang, Y. Zeng, Y. Bai, Z. Li, Y. Tian, and R. Li, "Coherent surface plasmon polariton amplification via free-electron pumping," Nature **611**, 55–60 (2022).
24. S. Kim, I.-K. Baek, R. Bhattacharya, D. Hong, M. Sattorov, A. Bera, J.-K. So, D.-S. Kim, and G.-S. Park, "High-*Q* metallic Fano metamaterial for highly efficient Cerenkov lasing," Adv. Opt. Mater. **6**, 1800041 (2018).
25. C. W. Hsu, B. Zhen, A. D. Stone, J. D. Joannopoulos, and M. Soljačić, "Bound states in the continuum," Nat. Rev. Mater. **1**, 16048 (2016).
26. K. L. Koshelev, Z. F. Sadrieva, A. A. Shcherbakov, Y. S. Kivshar, and A. A. Bogdanov, "Bound states in the continuum in photonic structures," Phys. Usp. **66**, 494–517 (2023).
27. D. C. Marinica, A. G. Borisov, and S. V. Shabanov, "Bound states in the continuum in photonics," Phys. Rev. Lett. **100**, 183902 (2008).
28. Y. Liang, K. Koshelev, F. Zhang, H. Lin, S. Lin, J. Wu, B. Jia, and Y. Kivshar, "Bound states in the continuum in anisotropic plasmonic metasurfaces," Nano Lett. **20**, 6351–6356 (2020).
29. Y. Tang, Y. Liang, J. Yao, M. K. Chen, S. Lin, Z. Wang, J. Zhang, X. G. Huang, C. Yu, and D. P. Tsai, "Chiral bound states in the continuum in plasmonic metasurfaces," Laser Photon. Rev. **17**, 2200597 (2023).
30. K. Hirose, Y. Liang, Y. Kurosaka, A. Watanabe, T. Sugiyama, and S. Noda, "Watt-class high-power, high-beam-quality photonic-crystal lasers," Nat. Photonics **8**, 406–411 (2014).
31. F. Wu, J. Wu, Z. Guo, H. Jiang, Y. Sun, Y. Li, J. Ren, and H. Chen, "Giant enhancement of the Goos-Hänchen shift assisted by quasi-bound states in the continuum," Phys. Rev. Appl. **12**, 014028 (2019).
32. E. Melik-Gaykazyan, K. Koshelev, J.-H. Choi, S. S. Kruk, A. Bogdanov, H.-G. Park, and Y. Kivshar, "From Fano to quasi-BIC resonances in individual dielectric nanoantennas," Nano Lett. **21**, 1765–1771 (2021).
33. H. Shu, L. Chang, Y. Tao, B. Shen, W. Xie, M. Jin, A. Netherton, Z. Tao, X. Zhang, R. Chen, B. Bai, J. Qin, S. Yu, X. Wang, and J. E. Bowers, "Microcomb-driven silicon photonic systems," Nature **605**, 457–463 (2022).
34. H. Zheng and H. U. Baranger, "Persistent quantum beats and long-distance entanglement from waveguide-mediated interactions," Phys. Rev. Lett. **110**, 113601 (2013).
35. J. Lee, B. Zhen, S.-L. Chua, W. Qiu, J. D. Joannopoulos, M. Soljačić, and O. Shapira, "Observation and differentiation of unique high-*Q* optical resonances near zero wave vector in macroscopic photonic crystal slabs," Phys. Rev. Lett. **109**, 067401 (2012).
36. Y. Song, N. Jiang, L. Liu, X. Hu, and J. Zi, "Cherenkov radiation from photonic bound states in the continuum: towards compact free-electron lasers," Phys. Rev. Appl. **10**, 064026 (2018).
37. C. Roques-Carmes, S. E. Kooi, Y. Yang, A. Massuda, P. D. Keathley, A. Zaidi, Y. Yang, J. D. Joannopoulos, K. K. Berggren, I. Kaminer, and M. Soljačić, "Towards integrated tunable all-silicon free-electron light sources," Nat. Commun. **10**, 3176 (2019).
38. J. F. Zhu, C. H. Du, F. H. Li, L. Y. Bao, and P. K. Liu, "Free-electron-driven multi-frequency terahertz radiation on a super-grating structure," IEEE Access **7**, 181184–181190 (2019).
39. A. E. Miroshnichenko, S. Flach, and Y. S. Kivshar, "Fano resonances in nanoscale structures," Rev. Mod. Phys. **82**, 2257–2298 (2010).
40. K. Koshelev, S. Lepeshov, M. Liu, A. Bogdanov, and Y. Kivshar, "Asymmetric metasurfaces with high-*Q* resonances governed by bound states in the continuum," Phys. Rev. Lett. **121**, 193903 (2018).
41. A. Szczepkowicz, L. Schächter, and R. J. England, "Frequency-domain calculation of Smith–Purcell radiation for metallic and dielectric gratings," Appl. Opt. **59**, 11146–11155 (2020).
42. H. F. Ma, X. Shen, Q. Cheng, W. X. Jiang, and T. J. Cui, "Broadband and high-efficiency conversion from guided waves to spoof surface plasmon polaritons," Laser Photon. Rev. **8**, 146–151 (2014).
43. X. Shen, T. J. Cui, D. Martin-Cano, and F. J. Garcia-Vidal, "Conformal surface plasmons propagating on ultrathin and flexible films," Proc. Natl. Acad. Sci. USA **110**, 40–45 (2012).
44. K. Sun, H. Wei, W. Chen, Y. Chen, Y. Cai, C.-W. Qiu, and Z. Han, "Infinite-*Q* guided modes radiate in the continuum," Phys. Rev. B **107**, 115415 (2023).
45. W. Wang, Y. K. Srivastava, T. C. Tan, Z. Wang, and R. Singh, "Brillouin zone folding driven bound states in the continuum," Nat. Commun. **14**, 2811 (2023).